Department of Complexity Science and Engineering
Graduate School of Frontier Sciences
The University of Tokyo

2020

Master's Thesis

Langmuir Probe Measurements of Scrape-Off Layer Conditions in Lower Hybrid Wave-driven Plasmas in TST-2

Submitted July 20, 2020

Supervisor: Lecturer Dr. Naoto Tsujii

ジェームズ　ハーミルトン　パーマー　ライス

James Hamilton Palmer Rice

Langmuir Probe Measurements of Scrape-Off Layer Conditions in Lower Hybrid Wave-driven Plasmas in TST-2

ジェームズ　ハーミルトン　パーマー　ライス

James Hamilton Palmer Rice

47-186155

Complexity Science and Engineering

Completed: September 2020

Keywords: *Fusion Energy, Langmuir Probes, Spherical Tokamak, Scrape-Off Layer, Lower-Hybrid Waves*

Abstract

A new Langmuir probe was designed and tested for use in the Scrape-Off Layer (SOL) region of the TST-2 spherical tokamak device. The probe area was increased from the previous design to improve signal clarity. Separate probes were included on both sides of the plasma limiter to identify asymmetry. Measurements of 1.0×10^{16} m^{-3} were obtained during LH-driven discharges at the lower limiter. The increased probe area gave better accuracy of electron density n_e measurements by improving the signal-to-noise ratio of ion saturation current. Bulk electron temperature T_e was found to be 8-10 eV without LH power, which increased to 20 eV during LH power. Floating potential V_{fl} was non-negative at the lower limiter, and showed positive correlation with injected LH power. The radial profile of plasma density at the bottom-limiter was estimated, with a decay length of about 60 mm, similar to previous results from the Outboard-antenna limiter. A non-thermal, linear component was observed in a particular discharge, which may correspond to a fast electron plateau caused by Lower-Hybrid Current Drive (LHCD).

Contents

1 Introduction **4**

1.1 The Necessity for Fusion Energy 4

1.2 Spherical Tokamak 5

1.3 Lower-Hybrid Current Drive 8

1.4 Thesis Objectives 10

2 Langmuir Probe Theory **11**

2.1 The I-V Characteristic 11

2.2 RF Sheath Rectification 16

2.3 Probe Measurements in Magnetized Plasma 16

3 Experimental Set-up **18**

3.1 The TST-2 Spherical Tokamak 18

3.2 Development of Langmuir Probe Diagnostic 18

3.2.1 Previously Installed Probes 20

3.2.2 New Probe Design 20

4 Experimental Results **23**

4.1 Typical Results of Plasma Parameters 23

4.2 Radial Profile Measurements 24

4.3 Influence of RF Power 32

4.4 Non-thermal I-V Response 34

4.4.1 Linear Offset Model 34

4.4.2 Source of the Non-thermal Component 36

5 Conclusions and Future Work **40**

A Derivation of the Langmuir Expressions for Probe Electron Current **42**

B Electron Energy Distribution Function Analysis **45**

Chapter 1

Introduction

1.1 The Necessity for Fusion Energy

Nuclear Fusion is the process in which lighter elements fuse to form heavier ones. It is the process that powers the sun, and in turn provides the vast majority of all energy ever consumed on Earth. Reactions release nuclear binding energy which can be captured to produce electricity, known as Fusion Energy. There is no chain reaction to lead to a core meltdown and little high-level radioactive waste is produced. As the climate crisis worsens and natural disasters become more common, a safe and sustainable alternative to fossil fuels is becoming increasingly necessary. While Nuclear Fission power can provide a carbonless alternative, it can lead to large and ongoing nuclear disasters such as Chernobyl and Fukushima Daiichi. Fusion Energy has no potential for such catastrophes. Better yet, Fusion has roughly 6 times greater energy yield by weight than uranium reactors, and a single kilo of deuterium can produce as much electricity as 7,000 tonnes of coal [1]. It is the responsibility of current generations to earnestly attempt to provide humanity with a safe, sustainable and economic source of power, which Fusion energy aims to supply.

Nuclei consist of nucleons - neutrons and protons - bound together by the short-range Nuclear Strong force. The latter of these are positively charged, meaning nuclei are strongly repelled by each other through Coulomb interaction. This

repulsion becomes stronger with proximity, but if brought close enough - within a nuclear diameter - the Nuclear Strong force will cause them to bind together in a fusion reaction. The resulting element has less total mass than the reactants, and the mass deficit is released as kinetic energy. The energy emitted can be used to drive a steam turbine generator to produce electricity through use of a thermal blanket.

The most accessible fusion reaction fuses the Hydrogen isotopes Deuterium D and Tritium T to produce Helium [1].

$$\mathrm{D} + \mathrm{T} \rightarrow {}^{4}\mathrm{He} + \mathrm{n} + 17.6\,\mathrm{MeV} \tag{1.1}$$

For D-T fusion, the optimum fuel temperature is 15-20 keV ($\approx$ 200 million °C). At these temperatures, chemical and atomic bonds break down, leading to the formation of plasma. Plasma is a mixture of negatively-charged electrons and positively-charged ions, and confining the high energy plasma poses a significant challenge. The daughter helium nuclei, also known as alpha particles, can be confined magnetically, while neutrons are quickly lost. Ideally, the heat captured from the helium's kinetic energy supplies the energy required to sustain the reaction temperature, which is known as ignition. There exists an ignition condition relying on the plasma density n and temperature T, as well as confinement time τ_E of [1]

$$nT\tau_E > 8.3\,\mathrm{atms}. \tag{1.2}$$

1.2 Spherical Tokamak

Magnetically confined fusion uses the combination of strong magnetic fields to isolate the hot core plasma from direct contact with the device's wall. Plasma consists of charged particles whose motion is governed by the Lorentz equation of electromagnetic force. Charged particles tend to follow magnetic field lines rather than move across them. Any motion perpendicular to the magnetic field causes centripetal acceleration by the Lorentz force, leading to a characteristic gyro-radius $\rho = m\upsilon_{\perp}/eB$. The presence of an electric field or inhomogeneity of

the magnetic field gives rise to drift velocities, namely $E \times B$, ∇B and curvature drifts [2]. By creating a toroidal (from torus, or donut-shaped) magnetic field, these particles are confined in the horizontal plane to lowest order, Fig. 1.1. However, the curved magnetic field causes the electrons and ions to drift vertically in opposite directions by the curvature and ∇B drifts. These cause charge separation such that the plasma drifts outwards by the $E \times B$ drift. The charge separation can be eliminated by the introduction of a poloidal (from polar-toroidal) magnetic field. The combination of these two creates helical field lines, which forms nested magnetic surfaces. The outer-most magnetic surface is known as the Last Closed Flux Surface (LCFS), within which core plasma is magnetically confined. Plasma outside of this region is unconfined, and is referred to as the Scrape-Off Layer (SOL). Finally, the application of a vertical magnetic field exerts an inward magnetic pressure on core plasma to balance outward plasma pressure. The ultimate result of these three field components (toroidal, poloidal and vertical) is a plasma which is fully confined. In a tokamak, the poloidal field is generated by the current carried by the plasma itself, whereas it is generated by external coils in stellarators. This forms the basis of toroidal magnetic confinement.

The stability of the tokamak plasma can be evaluated using Magneto-Hydro-Dynamics (MHD) [2], the result of which is that the plasma is more stable when magnetic field curvature faces towards the plasma. In the tokamak configuration, there is unfavourable curvature on the outboard (outer) side, and favourable curvature on the inboard (inner) side. One parameter describing the tokamak geometry is the aspect ratio: the ratio of the major radius R_0 and minor radius a of the torus ($A = R_0/a$). Tokamaks can be made more stable by reducing the aspect ratio, allowing for operation at a higher value of $\beta = 2\mu_0 p/B_t^2$: the ratio of magnetic and plasma pressures [3]. Spherical Tokamaks (ST) achieve an aspect ratio much lower than conventional tokamaks by operating at a lower magnetic field strength, leading to a compact tokamak.

Plasma current is most easily driven inductively using a Central Solenoid (CS) in the Center Stack of the tokamak device. Toroidal plasma current is induced in the plasma via a transformer action, which causes Joule heating through finite

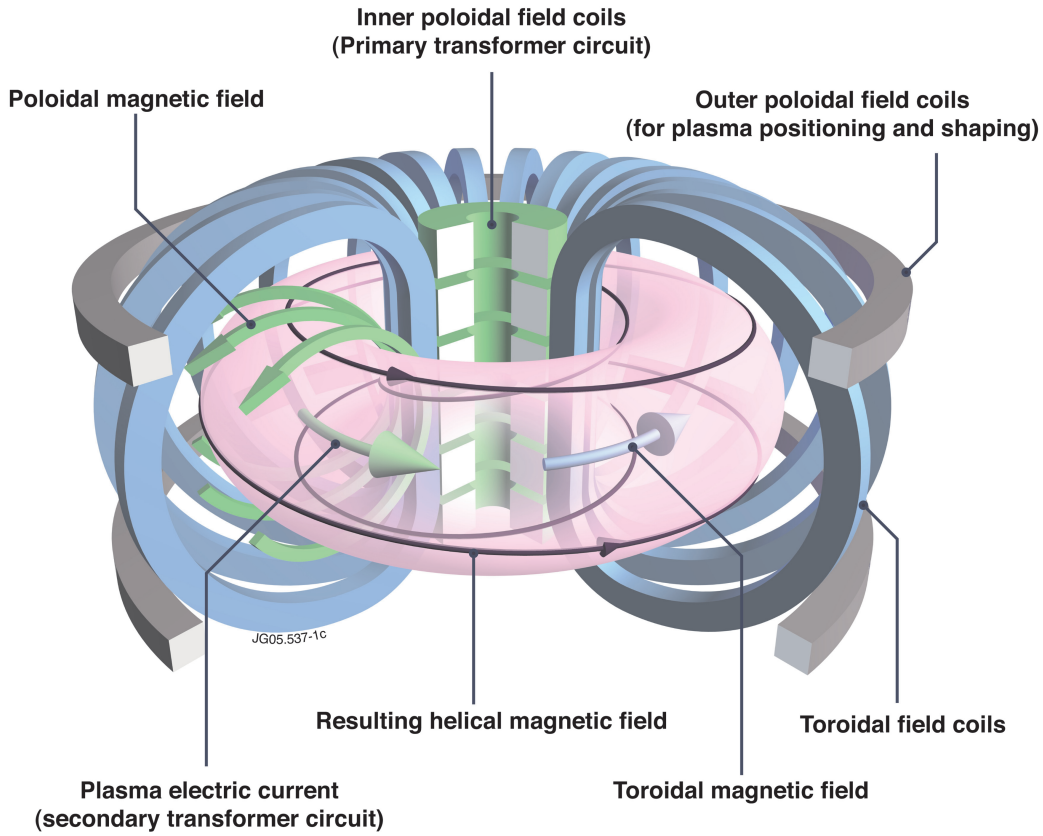

Figure 1.1: Schematic diagram of the tokamak configuration (reproduced from WikiCommons [4]), showing the plasma torus (pink), toroidal field coils and resulting field (blue), primary transformer, plasma current and resulting poloidal field (green).

plasma resistance. However, as the plasma temperature increases, the plasma resistance decreases and heating efficiency drops. Additionally, inductive heating cannot sustain a steady-state discharge. Furthermore, the CS takes up physical space in the Center Stack of the device, increasing the minimum aspect ratio and thereby limiting the confinement efficiency. For these reasons, inductive heating is easy to achieve, but is not ideal for use in a steady-state reactor.

In both conventional and spherical tokamaks, the non-inductive generation of toroidal current is a major and active field of research. There are a number of non-inductive means of heating and current drive in tokamak devices. These include Lower-Hybrid Current Drive (LHCD) [5], Neutral Beam Current Drive (NBCD), Electron Cyclotron Current Drive (ECCD), and the intrinsic Bootstrap Current of the device. Each method has its own advantages and disadvantages, and in many cases, they can be used in conjunction with each other and/or inductive heating. If these methods can be used instead of induction, the CS can be neglected. This would relax the space requirements in the Center Stack, leading to more compact devices. Realizing methods of fully non-inductive start-up, heating and current drive can be a cost effective pathway to economic fusion.

1.3 Lower-Hybrid Current Drive

Lower Hybrid Waves (LHW) are an effective method of current drive in plasma. The plasma conditions that allow for the propagation of LH Waves are given by the cold plasma dispersion relation [2]. Waves are injected at a frequency between the electron and ion cyclotron frequencies $\omega \sim \sqrt{\omega_{ce}\omega_{ci}}$. The LHW starts to propagate above the plasma cut-off density:

$$n = \frac{\omega^2 \epsilon_0 m_e}{e^2}, \tag{1.3}$$

which depends only on the injected wave frequency. For TST-2's 200 MHz system, this cut-off is at 0.5×10^{15} m^{-3}. There exists another branch at the same frequency condition, known as the 'fast' wave. The density at which the Lower Hybrid (or 'slow') and fast wave branches meet is called the 'mode conversion'

limit, above which LHW cannot propagate. At this limit, waves undergo mode conversion to the fast wave and return back towards the plasma periphery.

Lower-Hybrid Current Drive (LHCD) offers an efficient and effective method of driving toroidal plasma current I_p in a tokamak device [5]. The only mechanism of wave absorption at the wave frequencies in question is electron Landau damping, which accelerates electrons in the direction parallel to the magnetic field. Waves are injected with a directional wave-number, and are absorbed at wave-particle resonance: when the particle's velocity parallel to the magnetic field is equal to the parallel phase velocity of the wave $v_{\parallel} = \omega/k_{\parallel}$. Electrons near the phase velocity $v_{\parallel}$ of the wave exchange energy with the wave: slower particles gain energy and faster particles lose energy. For a Maxwellian distribution, there are more particles slower than the wave, and a net transfer of energy to the electrons occurs. This acts to flatten the electron distribution, producing a high energy 'tail'. Due to the asymmetric velocity distribution of the wave, electrons also obtain momentum from the wave, generating current. It is the suprathermal tail electrons that carry most of the current. As long as power is injected, this flattening of the distribution is maintained and current sustained; but once power stops, the high energy electrons thermalize into the bulk through Coulomb collisions. Because collision frequency $\nu_{ei} \propto 1/v_e^3$ is reduced at higher velocities, the tail electrons experience less Coulomb collisions than the bulk, leading to high current drive efficiency.

Current drive efficiency decreases at higher plasma density. Experiments on many devices [6–8] have indicated steeper loss of current drive efficiency than theoretical models suggest [5]. The cause of this anomalous loss of efficiency is not yet fully understood and further research is necessary to identify the cause(s). Previously identified sources of power loss include SOL power absorption [9], collisional processes [10], parametric decay instability [6], and SOL density fluctuations [11]. Many of these potential losses involve wave interaction with SOL plasma, which has yet to be studied in depth in TST-2. Thus, a full profile of SOL plasma in the TST–2 spherical tokamak is desired to investigate the effect of these processes on the LHCD scenario.

1.4 Thesis Objectives

In order to meet required confinement conditions, LHW are an attractive current drive method. Understanding the limitations of LHCD is an important step towards this, and a full profile of SOL plasma is needed. To this end; this thesis aims to design, develop and test a new Langmuir probe diagnostic for the TST-2 device. The new probe aims to provide accurate and reliable measurements of plasma conditions in the SOL region. A more comprehensive profile of SOL plasma will assist in future research on non-inductive start-up and LHW physics.

Chapter 2

Langmuir Probe Theory

The Langmuir probe has been described as the 'work horse' of measurements in Tokamak edge plasma and is a fundamental diagnostic tool in low temperature plasmas [12, 13]. The basic concept and implementation is simple [14] but requires detailed analysis. A conductive probe tip is placed in plasma and allowed to accumulate charge from the plasma. If a bias voltage is applied, oppositely charged particles are screened from approaching the probe. If this voltage is swept, a current response is produced, which can be measured across a pickup resistor. The characteristic Current-Voltage (I-V) response is related to the plasma conditions of electron temperature T_{e}, density n_{e} and potential V_p. If the sweep frequency is sufficiently fast, near continuous measurements of these parameters can be obtained. This makes the Langmuir Probe a very powerful diagnostic tool if used appropriately. There are three main modes of operation when using a Langmuir Probe: the single-, double-, and triple-probe configurations: this thesis focuses on the use of single-probes.

2.1 The I-V Characteristic

To begin constructing the collisionless I-V response of a probe in plasma, we shall consider a negatively biased probe tip so that ions are attracted and electrons repelled. If the bias is sufficiently negative compared to the plasma potential

V_p, almost all electrons are screened and a region of reduced electron density forms. This region of perturbed plasma, referred to as the sheath, does not extend infinitely: only a small distance away from the probe. This sheath width is typically a few Debye lengths $\sim 4\lambda_{\mathrm{D}}$, and in fusion plasmas is typically tens of μm thick. The electron density is approximated by the electron density of unperturbed plasma far from the probe scaled by the Boltzmann factor:

$$n_e(x) \approx n_\infty \exp\left(\frac{e(V(x) - V(0)}{k_b T_{\mathrm{e}}}\right) \tag{2.1}$$

with n_{e} at a distance x from the probe being roughly exponential using plasma potential as reference $V_p = 0$ (Fig. 2.1). This thesis will take $k_b = 1$ and express temperature in terms of energy (1 K = k_b J). It is easily noticed that the condition of the probe being sufficiently negative is satisfied when the probe potential $|V| = V(x) - V(0) \gg T_{\mathrm{e}}/e$.

If ion and electron temperature are similar $T_{\mathrm{e}} \sim T_{\mathrm{i}}$, the ion thermal velocity is smaller by a factor of $\sqrt{m_{\mathrm{i}}/m_{\mathrm{e}}}$. For the following derivation, ion temperature contributions are neglected ($T_{\mathrm{i}} = 0$), but numerical solutions have shown that the result is mostly unchanged even for the $T_{\mathrm{e}} \sim T_{\mathrm{i}}$ case [12, 13]. For $T_{\mathrm{i}} = 0$, ion motion towards the probe is caused by sheath potential V_s alone,

$$|v_{\mathrm{i}}| = \sqrt{\frac{-2eV_{\mathrm{s}}}{m_{\mathrm{i}}}} \tag{2.2}$$

giving ion density flux of $\Gamma_{\mathrm{i}} = n_{\mathrm{i}} v_{\mathrm{i}}$. At equilibrium, this is constant, giving a total ion current density to a probe of surface area A:

$$J_{\mathrm{i}} = A n_{\mathrm{i}} v_{\mathrm{i}} = \text{const.} \tag{2.3}$$

Using (2.1)-(2.3) in Poisson's equation then gives

$$\nabla^2 V = \frac{-e}{\epsilon_0}\left[n_{\mathrm{i}} - n_{\mathrm{e}}\right] = \frac{-e}{\epsilon_0}\left[\frac{J_{\mathrm{i}}}{A}\sqrt{\frac{m_{\mathrm{i}}}{-2eV}} - n_\infty \exp\left(\frac{eV}{T_{\mathrm{e}}}\right)\right] \tag{2.4}$$

This has two main regions of interest: a quasineutral region known as the pre-sheath where $n_{\mathrm{e}} - n_{\mathrm{i}} \ll n_{\mathrm{e}}$, and the sheath region where quasineutrality is violated. In the pre-sheath where $n_{\mathrm{e}} \sim n_{\mathrm{i}}$,

$$n_\infty \exp\left(\frac{eV}{T_{\mathrm{e}}}\right) = \frac{J_{\mathrm{i}}}{A}\sqrt{\frac{m_{\mathrm{i}}}{-2eV}}. \tag{2.5}$$

Differentiating this reveals a dV/dx term with a coefficient of

$$n\left(\frac{e}{T_\mathrm{e}}+\frac{1}{2V}\right). \tag{2.6}$$

When this term is zero, the potential would have an infinite derivative. This means that the quasineutral assumption must break down and form a sheath when

$$V_s \geqslant -\frac{T_\mathrm{e}}{2e}. \tag{2.7}$$

In the sheath region, a planar approximation neglecting probe area dependence can be made, and the lowest order Taylor expansion results in

$$\nabla^2 V = -\frac{en_\mathrm{s}}{\epsilon_0}\left[-\frac{1}{2V_s}-\frac{e}{T_\mathrm{e}}\right](V-V_\mathrm{s}) \tag{2.8}$$

which has a single exponential solution when

$$V_\mathrm{s} \leqslant -\frac{T_\mathrm{e}}{2e}. \tag{2.9}$$

To satisfy continuity between the sheath and the pre-sheath, the sheath potential must be given exactly by

$$V_\mathrm{s} = -\frac{T_\mathrm{e}}{2e}. \tag{2.10}$$

This is the Bohm condition of sheath formation, and is maintained for any plasma at equilibrium with an insulating surface. If the probe potential were the same as the plasma, negative charge would build up due to the larger electron velocity compared to ion velocity. Thus, electrons are repelled and a positively charged sheath region forms. For the sheath to be positively charged, the sheath ion density n_is must exceed the sheath electron density n_es. There must be some minimum current density $n_\mathrm{i}v_\mathrm{i}$ at the sheath edge, and given that n_i is finite, this flux is caused by a minimum v_i caused by ions accelerated by the sheath potential V_s while crossing the pre-sheath. The ion flux density to a sufficiently negative probe tip is therefore

$$\Gamma_\mathrm{i} = n_\infty \exp\left(\frac{eV_s}{T_\mathrm{e}}\right)\sqrt{-\frac{2eV_s}{m_\mathrm{e}}} = \exp\left(-\frac{1}{2}\right)n_\mathrm{e}\sqrt{\frac{T_\mathrm{e}}{m_\mathrm{i}}}. \tag{2.11}$$

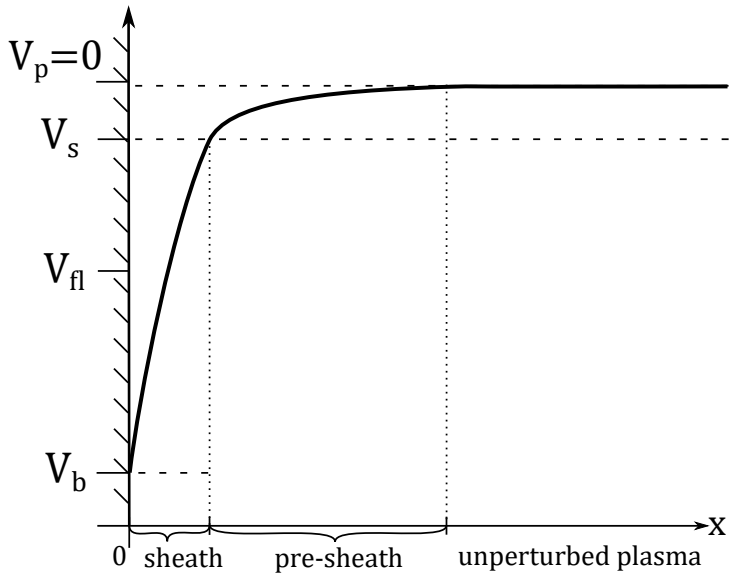

Figure 2.1: Potential schematic of Langmuir probe operation, showing probe bias V_b, sheath potential V_s and floating potential $V_{\rm fl}$ relative to plasma potential V_p ($V_b < V_{\rm fl}$ in this diagram).

The probe current under this condition is called the ion saturation current $I_{\rm sat}$ given by,

$$I_{\rm sat} = eAn_{\rm e}\exp\left(-\frac{1}{2}\right)\sqrt{\frac{T_{\rm e}}{m_{\rm i}}} = eAn_{\rm e}\exp\left(-\frac{1}{2}\right)C_s. \tag{2.12}$$

where C_s is the ion sound speed.

As the probe potential increases, so too does the population of electrons able to pass through the sheath and be collected by the probe. Close to the plasma potential, the electron current is much larger than the ion current, and can easily damage the probe through particle and heat flux. Excessive probe current can also perturb the measured plasma, which is undesirable. However, when the electron current is equal to $I_{\rm sat}$, no probe current is drawn. This is known as the probe floating potential $V_{\rm fl}$, and is the potential relative to the plasma potential $V_{\rm p}$ an insulated surface will naturally tend towards. Below this potential, electron flux is given by

$$\Gamma_{\rm e} = \frac{1}{4}n_\infty\bar{v}_{\rm e}\exp\left(\frac{eV}{T_{\rm e}}\right) = n_{\rm e}\sqrt{\frac{T_{\rm e}}{2\pi m_{\rm e}}}\exp\left(\frac{eV}{T_{\rm e}}\right) \tag{2.13}$$

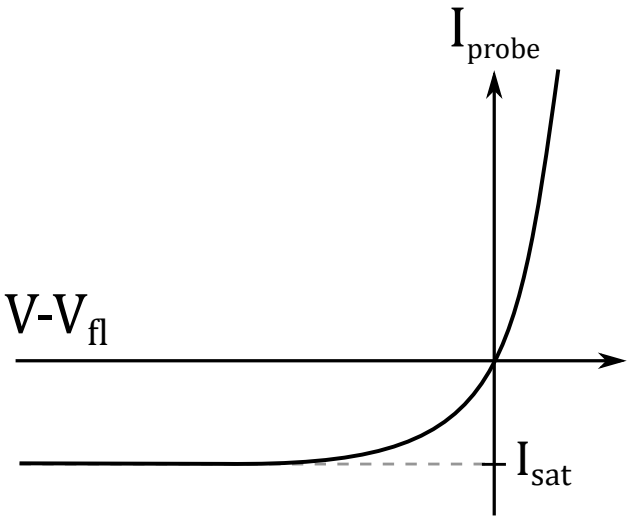

Figure 2.2: The I-V Characteristic of a Langmuir probe around the floating potential, identifying ion saturation current I_{sat}.

where $\bar{v}_{\text{e}} = \sqrt{8T_{\text{e}}/\pi m_{\text{e}}}$. For probe potentials below or near V_{fl} in thermal plasma, probe current I_{probe} is then

$$I_{\text{probe}} = eAn_{\text{e}}\sqrt{\frac{T_{\text{e}}}{m_{\text{i}}}}\left[\exp\left(-\frac{1}{2}\right) - \frac{1}{2}\sqrt{\frac{2m_{\text{i}}}{\pi m_{\text{e}}}}\exp\left(\frac{eV}{T_{\text{e}}}\right)\right] \tag{2.14}$$

This characteristic curve can be seen in Fig. 2.2. Electron temperature T_{e} can be found from the exponential curve, and plasma density $n \approx n_{\text{e}}$ then calculated using ion saturation current I_{sat}.

The plasma potential V_p can be calculated from the probe floating potential. By setting $\Gamma_{\text{i}} = \Gamma_{\text{e}}$ and reintroducing V_p, one can obtain the result presented in [12]:

$$\frac{e\left(V_{\text{fl}} - V_p\right)}{T_{\text{e}}} = \frac{1}{2}\left[ln\left(\frac{2\pi m_{\text{e}}}{m_{\text{i}}}\right) - 1\right] \tag{2.15}$$

This can be expressed in the form

$$V_{\text{fl}} = V_p - \frac{\Lambda T_{\text{e}}}{e} \tag{2.16}$$

where Λ is the plasma sheath coefficient and is approximately 3.3 in H plasma, 3.7 in D plasma, and 3.8 in D-T plasma. The inclusion of finite T_{i} causes Λ

to decrease [12, 13], but only weakly. Experimental results of Λ obtained in fusion devices [15–18] indicate that $\Lambda \approx 3$ is a generally good approximation in D plasma.

2.2 RF Sheath Rectification

The fluctuation of plasma potential by Radio Frequency (RF) waves causes the floating potential to decrease, which is known as RF sheath rectification. This can be accounted for by the addition of an oscillatory potential $V_{\mathrm{RF}} \cos \omega t$ to the plasma potential V_p and averaging over RF oscillations [19]. The I-V response then becomes

$$\langle I(V) \rangle_{\mathrm{RF}} = I_{\mathrm{sat}} \left(1 - \exp \left(\frac{V + V_{\mathrm{fl}}^{\mathrm{RF}} - V_{\mathrm{fl}}^{\mathrm{noRF}}}{T_{\mathrm{e}}} \right) \right) \tag{2.17}$$

where

$$V_{\mathrm{fl}}^{\mathrm{RF}} = T_{\mathrm{e}} \ln \left[I_0 \left(\frac{V_{\mathrm{RF}}}{T_{\mathrm{e}}} \right) \right] \tag{2.18}$$

and I_0 is the modified Bessel function. Due to the non-linear I-V response, a positive fluctuation in potential produces a larger change in the probe current than a negative one, resulting in an increase in the time averaged probe current. The resulting I-V characteristic shows a floating potential V_{fl} lowered by $V_{\mathrm{fl}}^{\mathrm{RF}}$, as shown in Fig. 2.3.

2.3 Probe Measurements in Magnetized Plasma

Langmuir probe analysis can become complicated by the inclusion of a magnetic field. Charged plasma particles in a magnetic field orbit around field lines, travelling in helical paths characterized by the gyro- or Larmour radius $\rho = mv_{\perp}/eB$. The lighter electron mass results in $\rho_e < \rho_i$ by a factor of $\sqrt{m_{\mathrm{e}}/m_{\mathrm{i}}}$. If cross field motion is restricted on the probe scale, particle motion becomes roughly one-dimensional along the magnetic field. The usual collisionless theory of probe electron collection breaks down, and no solution to Eq. (2.8) is found without accounting for diffusive effects. Most fusion devices use probe dimensions such

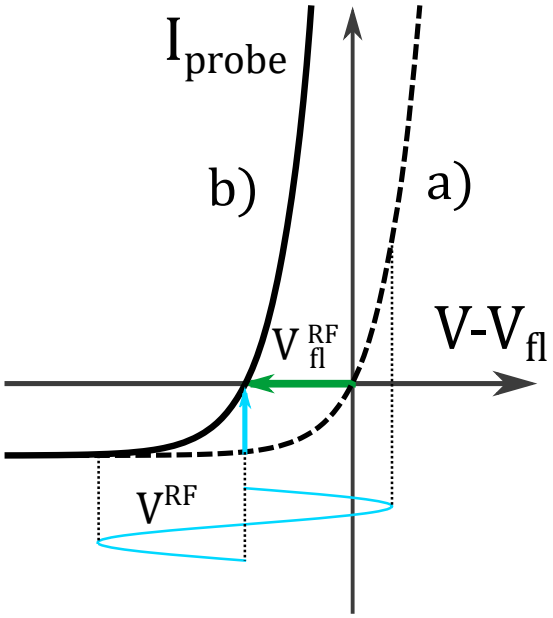

Figure 2.3: Schematic of RF sheath rectification showing a) original I-V characteristics and b) the corresponding rectified curve.

that $\rho_e \ll a < \rho_i$, causing electron collection on the probe scale to be strongly inhibited, but ion collection to be largely unchanged [20]. If sufficient cross field diffusion is present, the electron current is also unaffected, and the I-V characteristic presented above is still valid.

Chapter 3

Experimental Set-up

3.1 The TST-2 Spherical Tokamak

TST-2 is a spherical tokamak device at the University of Tokyo [21], see Fig. 3.1. TST-2 is equipped with a CS for conventional inductive operation. Auxiliary heating power in the form of ECH and LHCD is also available. The LH system operates at 200 MHz and is injected via two Capacitively Coupled Combline antennae located at the outboard and top sides of the plasma (see Fig. 3.2 a)). These can provide 200 kW and 100 kW of LH power, respectively. Fully non-inductive discharges are possible, in which breakdown is achieved using ECH power, and plasma current is driven by LHCD launched from the Outboard-antenna, which can then be handed over to the Top-antenna if desired. Discharges are referred to as Outboard- and Top-launch discharges depending on which antenna is used to sustain flat-top power. Typical operational conditions are given in Table. 3.1.

3.2 Development of Langmuir Probe Diagnostic

A new Langmuir probe was designed and implemented in TST-2's SOL plasma. Previous Langmuir probes had been installed on the plasma limiters of the Top- and Outboard-antennae for the measurement of plasma density in front of the antennae. Results from these previously installed probes were used to inform the

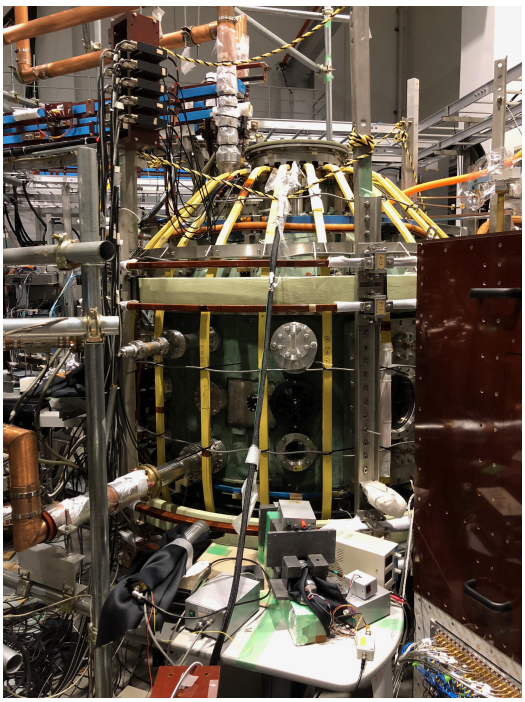

Figure 3.1: The TST-2 spherical tokamak device.

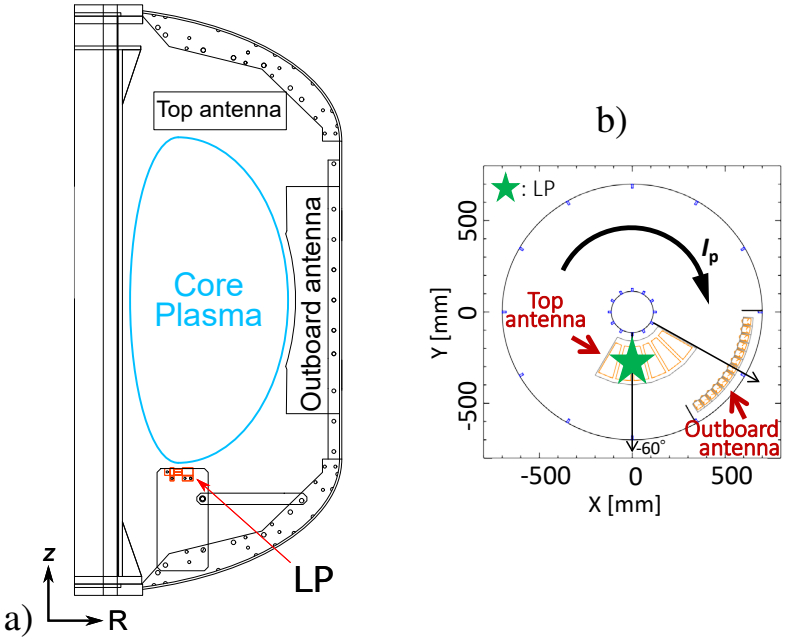

Figure 3.2: a) Poloidal and b) toroidal location of the new probe. Reproduced from Plasma Fus. Res. **15** 2402009 (2020) [22].

	OH	LH
Major radius	0.36 m	
Minor radius	0.23 m	
Toroidal field	<0.3 T	<0.16 T
Plasma current	<120 kA	<27 kA
Plasma density	$\sim 10^{19}$ m^{-3}	$\sim 10^{18}$ m^{-3}
Electron temp.	<400 eV	<50 eV

Table 3.1: Operational conditions of TST-2. OH and LH refer to discharges driven by the CS and LH, respectively.

new design. The goal of the new design was to increase the sensitivity of density measurements and obtain additional information on the asymmetry of the electron velocity distribution.

3.2.1 Previously Installed Probes

Probes previously used in TST-2 were installed on the Top- and Outboard-antenna limiters, and had probe areas of 20 and 40 mm^2, respectively. These probes were made of copper sheets housed in stainless steel mounts, and were insulated using machinable ceramic, as seen in Fig. 3.3. The probes drew ion saturation currents of about 0.5-1 mA, indicating a plasma density of less than 10^{16} m^{-3} directly in front of either antenna. This was comparable to the typical background noise level during discharges, which was about 1 mA. This required that I-V characteristics be averaged over many sweeps, limiting the time resolution of each measurement.

3.2.2 New Probe Design

With the above considerations in mind, a new probe was designed and is shown in Fig. 3.4a). This design featured 4 probe plates. Each probe plate was isolated from the stainless steel cover plate with spacers made of machinable ceramic. The probe was assembled using a clamping method whereby the probe plates and spacers were held fast by the stainless steel cover. The previous Top-antenna

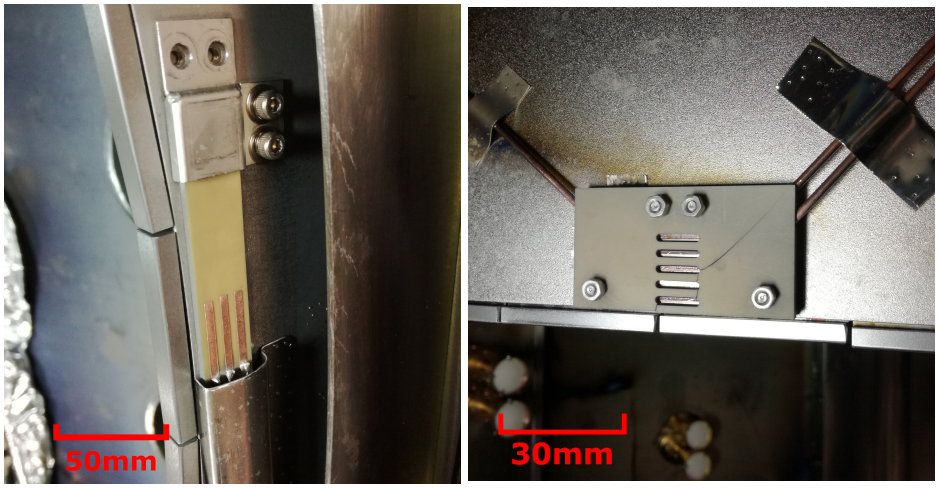

a) b)

Figure 3.3: Langmuir probes previously used in TST-2, attached to a) Outboard- and b) Top-antenna limiters. Note the cracked ceramic insulation in b).

probe in Fig. 3.3 b) used the ceramic plate to directly hold the probe plate and the coaxial cable in place, the pin-point stress of which caused a crack to appear as shown. Clamping spreads the force required to hold the probes in place in the strong magnetic fields present over a larger area, greatly reducing pinpoint stress and avoiding damage to ceramic parts. The area of each probe was increased to 20×6 mm = 120 mm^2 to increase the current signal. This increased the sensitivity of probe current by ~6 times, greatly improving the signal-to-noise ratio.

A large alteration in probe signal was observed during RF power, the main mechanism of which is not yet known. The change in electron temperature and floating potential indicated direct influence by RF power. Previous probe measurements showed that downstream probes were more strongly affected by RF power than upstream probes. This indicated asymmetry in the electron energy distribution. The new design featured probes on either side of the limiter in the hope that such asymmetry could be detected. Since the large alteration of the floating potential by RF sheath rectification can cause difficulty in taking measurements with the present power supply set-up, the new probe was moved away from the two RF antennae. The location chosen was roughly the midpoint of the Bottom-

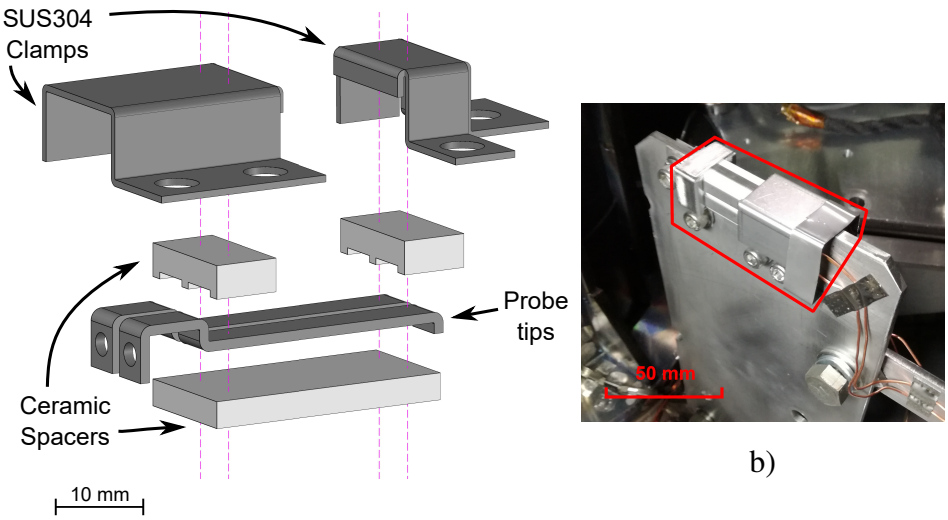

a) b)

Figure 3.4: a) Exploded design concept and b) probe installed on Bottom-limiter. Reproduced from Plasma Fus. Res. **15** 2402009 (2020) [22].

limiter, as shown in Fig. 3.2, (R, Z)=(275 mm, -450 mm). The radial profile of the plasma was not known at this position, so two probes were included on each side to estimate the radial profile. Probe plates were arranged horizontally, with probe midpoints spaced 5 mm and 13 mm from the limiter edge. This placed them perpendicular to the toroidal magnetic field, preventing alteration of the probe area projected along the magnetic field. The local value of the magnetic field at this location was 0.21 T during LH discharges. This corresponded to Larmor radii of $\rho_e = 36\ \mu m \ll \rho_i = 2.6$ mm at $T_e = T_i = 10$ eV. As ρ_i is comparable to the probe size (~6 mm), magnetic influence on probe measurements was not expected to be significant.

Chapter 4

Experimental Results

4.1 Typical Results of Plasma Parameters

Results obtained from previously installed probes, attached to the upstream side of Outboard- and Top-antenna limiters, are presented in Figs. 4.1 and 4.2 using the analytic model described in Sec. 2.1. The probe features two plates on both sides, with midpoints 9 mm and 17 mm, and 8 mm and 16 mm from the limiter edge for the Outboard- and Top-limiter probes, respectively. Measurements were obtained during Top-launch discharges, and probe bias voltage was applied relative to machine ground using a sweep frequency of 1 kHz and a sample frequency of 1 MHz; giving 1000 samples/sweep. Plasma densities of about 3×10^{15} m^{-3} were observed in both probes, which are in close agreement with previously published measurements [23]. I-V characteristics for the two probes during both Outboard- and Top-antenna power are shown in Figs. 4.3 and 4.4. Ion saturation current is fitted well for the Outboard-limiter probe, giving a good indication of density. However, large spikes in the current signal were observed when the antenna next to a probe was energized, making electron temperature and floating potential measurements inaccurate due to poor fitting. The probes measured electron temperatures of about 40 eV when the antenna away from the probes was energized. While fitting indicated a negative floating potential during the Outboard-antenna driven phase (<30 ms), direct observation of the I-V curves determined that floating po-

tential was actually somewhat positive. Ion saturation current was also well-fitted for the Top-limiter probe during Outboard-antenna power, but the probe drew a positive probe current during Top-antenna power. This showed that the I-V characteristic had been strongly altered by RF sheath rectification in this time period, as described in Sec. 2.2. This had caused electron current to be drawn for the entire bias sweep. The floating potential of the Top-limiter probes was found to be near zero during Outboard-antenna power.

Results of measurements taken during both Top- and Outboard-launch discharges using the new probe located at the Bottom-limiter are shown in Figs. 4.5 and 4.6, respectively. The accuracy of density measurements in TST-2's low density SOL was improved upon by increasing the surface area of the new probe. Flat-top power values of electron density were found to be 1.0×10^{16} m^{-3} during both Outboard- and Top-launch discharges. This is somewhat larger than measurements using the previously installed probes on the Outboard- and Top-limiters. Corresponding I-V characteristics taken during flat-top RF power from both the Top- and Outboard-antennae are shown in Fig. 4.7. I-V characteristics were well fitted, with ion saturation current reached in all cases. The floating potential was found to be positive during operation of either antenna, with downstream probes having a higher floating potential during both antenna phases. The positive floating potential in both probes indicates that RF sheath rectification has been largely avoided at the new probe's location.

4.2 Radial Profile Measurements

The radial separation of two probes allowed for the radial plasma profile to be estimated. Ion saturation currents were measured using both probes with a static -140 V bias, with probe midpoints 5mm and 13 mm from the limiter edge. Assuming the temperature at the two locations was the same, this was proportional to density. The ratio of the two was used to calculate the density decay length λ assuming an exponential decay profile

$$n(r) = n_0 \exp\left(\frac{-r}{\lambda}\right), \tag{4.1}$$

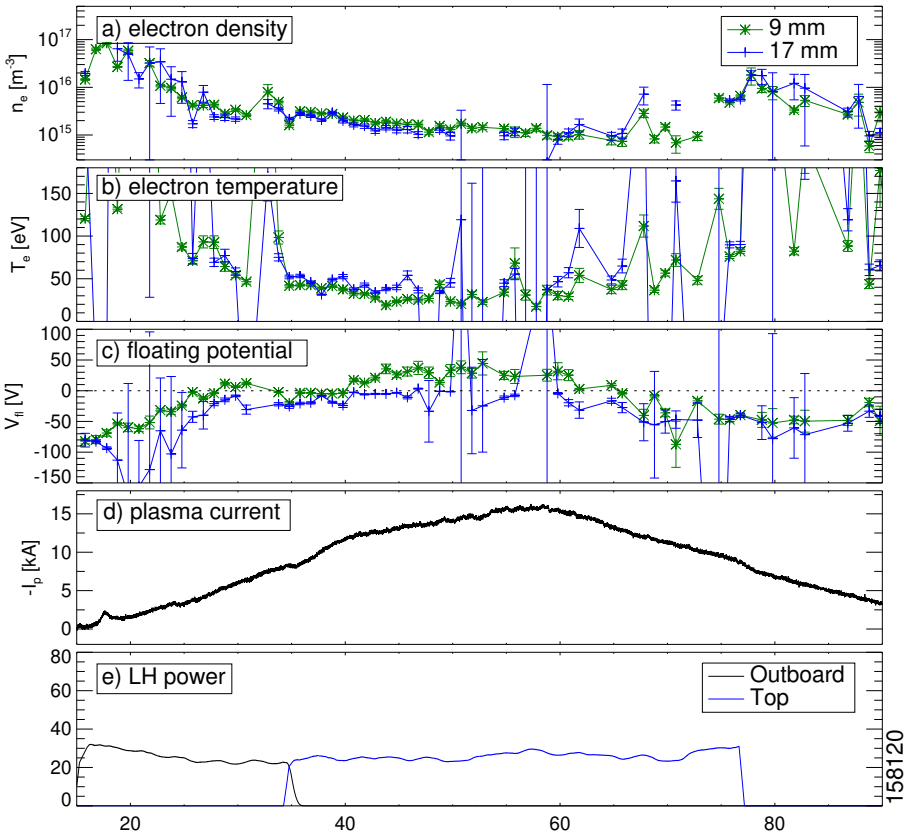

Figure 4.1: Langmuir Probe measurements from the previous probe installed on the upstream Outboard antenna limiter (shot #158120). Plasma conditions of a) electron density n_e, b) electron temperature T_e and c) probe floating potential V_{fl} are presented for probes 9 mm (green) and 17 mm (blue) from the limiter edge, as well as d) plasma current I_p and e) injected LH power from the Outboard- and Top-antennae in black and blue, respectively.

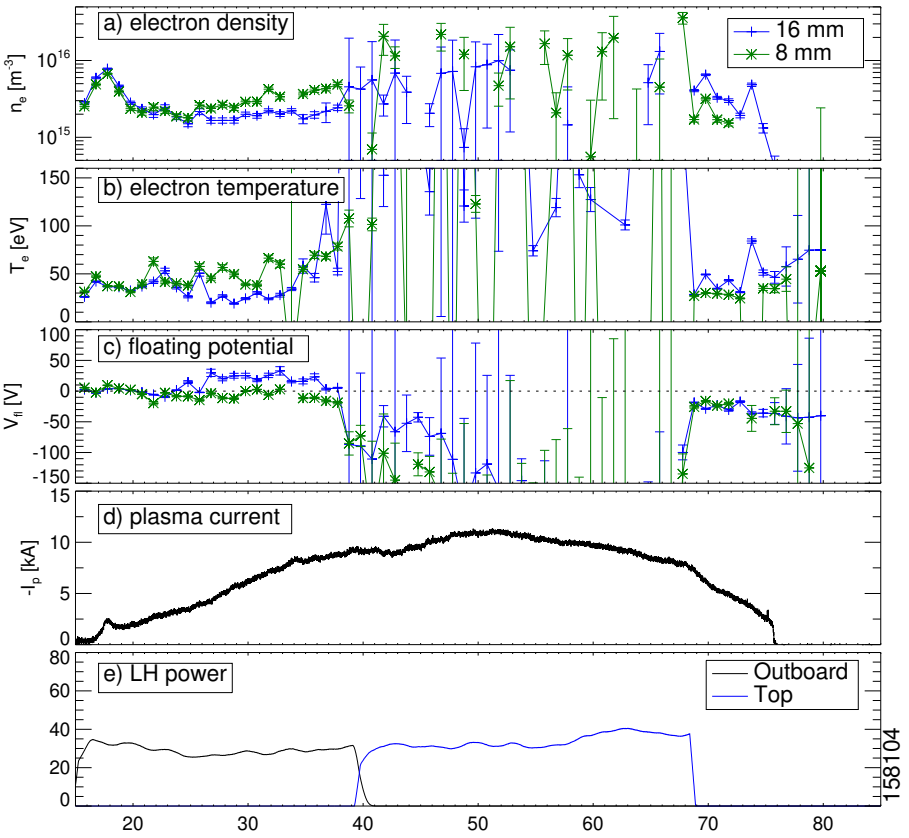

Figure 4.2: Langmuir Probe measurements from the previous probe installed on the upstream Top antenna limiter (shot #158104). Plasma conditions of a) electron density n_e, b) electron temperature T_e and c) probe floating potential V_{fl} are presented for probes 8 mm (green) and 16 mm (blue) from the limiter edge, as well as d) plasma current I_p and e) injected LH power from the Outboard- and Top- antennae in black and blue, respectively.

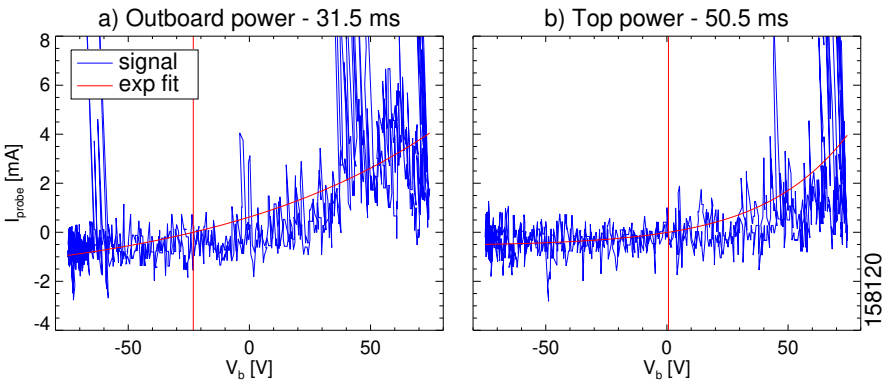

Figure 4.3: Fitted I-V characteristics from shot #158120 (Fig. 4.2) during a) Outboard- and b) Top-antenna power using an exponential fitting model.

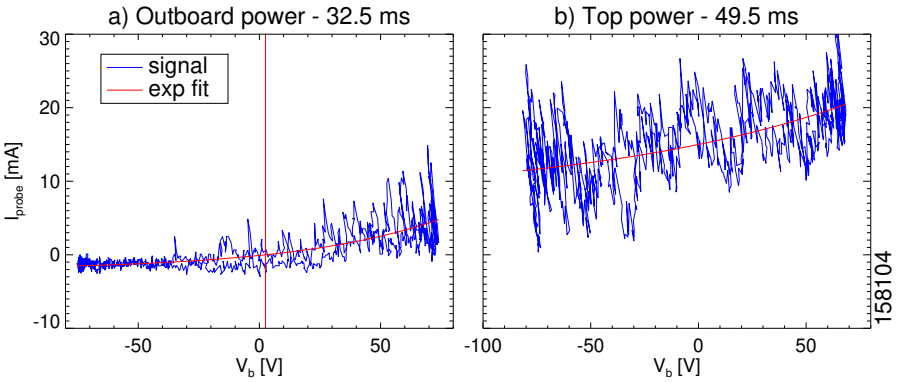

Figure 4.4: Fitted I-V characteristics from shot #158104 (Fig. 4.1) during a) Outboard- and b) Top-antenna power using an exponential fitting model.

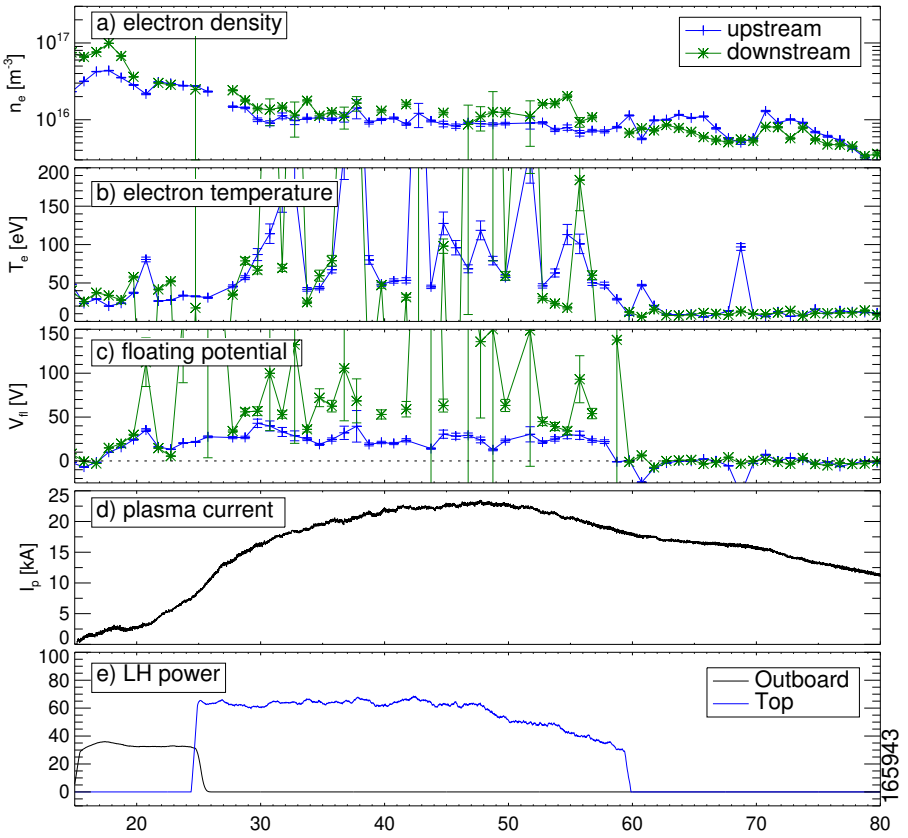

Figure 4.5: Langmuir Probe measurements from the new probe installed on the Bottom-limiter taken during Top-launch discharge (shot #165943). Plasma conditions of a) electron density n_e, b) electron temperature T_e and c) probe floating potential V_{fl} are presented for both upstream (blue) and downstream (green) probes, as well as d) plasma current I_p and e) injected LH power from the Outboard- and Top- antennae in black and blue, respectively.

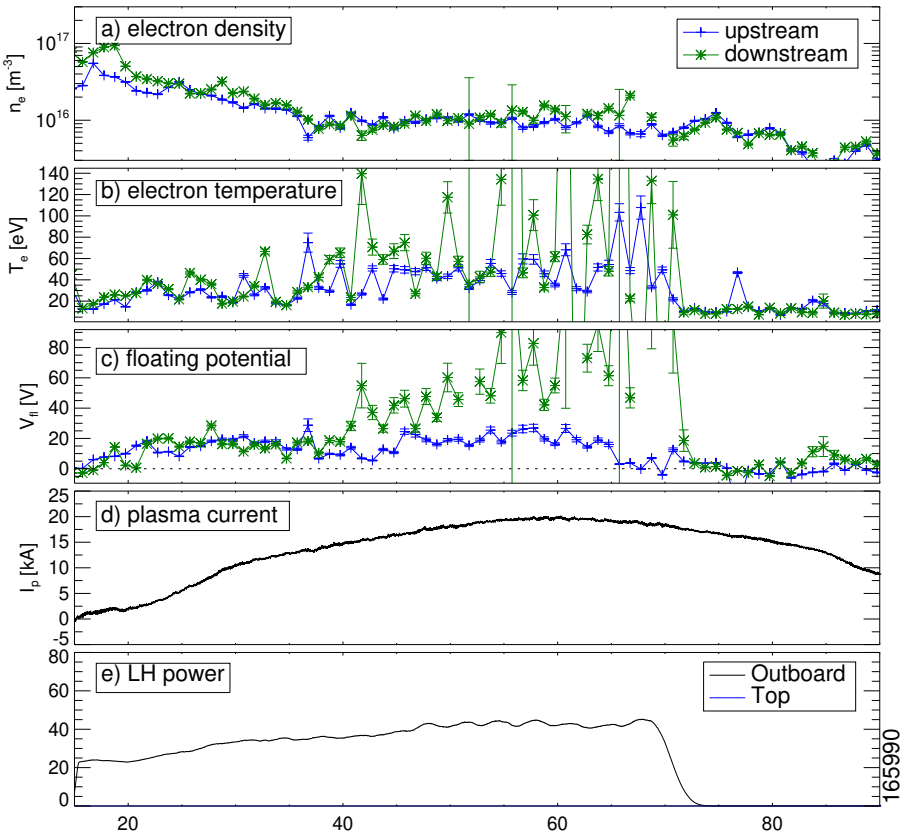

Figure 4.6: Langmuir Probe measurements from the new probe installed on the Bottom-limiter taken during Outboard-launch discharge taken during Top-launch discharge (shot #165990). Plasma conditions of a) electron density n_e, b) electron temperature T_e and c) probe floating potential V_{fl} are presented for both upstream (blue) and downstream (green) probes, as well as d) plasma current I_p and e) injected LH power from the Outboard- and Top- antennae in black and blue, respectively.

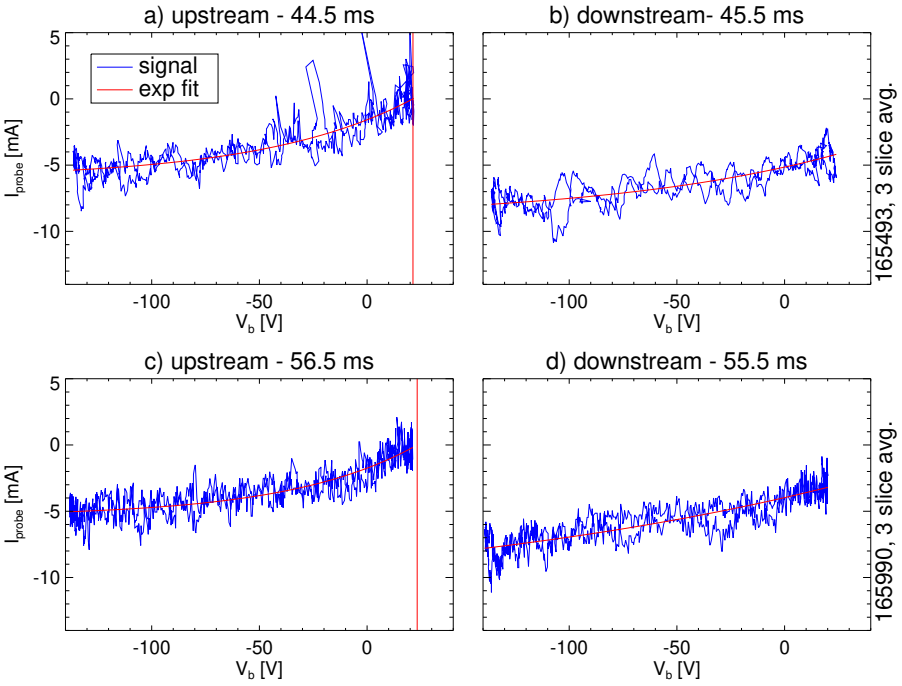

Figure 4.7: Fitted I-V characteristics taken by the new probe during a-b) Top- and c-d) Outboard-antenna power for the upstream and downstream probes, respectively. Curves shown are an average of 3 voltage sweeps.

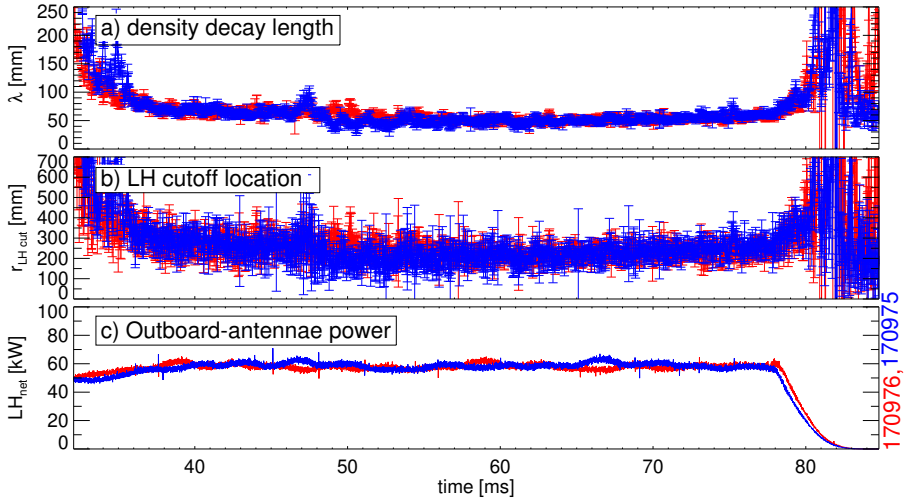

Figure 4.8: Results of a) density decay length λ and b) LH cutoff location calculated from ion saturation current using probes 8 mm and 13 mm from the limiter edge, both with (blue) and without (red) a gas puff at 45 ms (shots #170976 and #170975), and c) injected Outboard-antenna power.

where n_0 is the plasma edge density and r is the distance from the plasma edge. The penetration depth of LHW was also found by extrapolating to the radial position where the LHW cut-off density was reached by

$$r_{\text{cutoff}} = \lambda \ln\left(\frac{n_{\text{cutoff}}}{n}\right) + r_0 \tag{4.2}$$

where r_0 is the probe distance from the limiter edge and n is the density measured by the probe. These results are presented in Fig. 4.8.

Decay lengths during flat-top were found to be 60-80 mm. These measurements agree with previous results of radial density decay found using the Outboard-limiter probe [24]. This corresponded to a penetration length of 20-40 cm from the limiter edge. A gas puff was introduced at around the beginning of the flat-top phase (45 ms) to see the impact on the SOL density. No clear difference was seen between the discharges with and without a gas puff in this experiment. Future probes should include three or more radial locations to allow for exponential fitting, as well as more poloidal locations to investigate any poloidal variation in the

profile.

4.3 Influence of RF Power

The dependence of plasma conditions on RF power was investigated by varying the magnitude of injected LH power across discharges. The experiment used a Top-launch discharge which varied flat-top power from 10 kW to 90 kW (ramp up), and vice versa (ramp down). The results of the experiments are shown in Fig. 4.9. These showed correlation between injected power and probe floating potential. As injected power was ramped, the floating potential signals showed positive correlation with injected power. The floating potential and the ion saturation current were plotted against RF power, as shown in Fig. 4.10, which showed correlation between injected RF power and the floating potential. The correlation in the density signal was weak; density converged at an earlier time before decreasing independently of RF power.

To further isolate the time dependent response of the SOL conditions to RF power, a fast square-wave modulation was applied to the RF power at 1 kHz (60% duty). The Top-launch antenna was used for this experiment, and the results are shown in Fig. 4.11. A modified fitting model was used for this discharge for reasons which will be described later in Sec. 4.4.1. The RF switching width was 20-40 μs, and bias sweeps were performed at 40 kHz with a 2 MHz sampling frequency, corresponding to an individual time resolution of 25 μs. A boxcar averaging of 3 sweeps was applied. The RF switching was nearly instantaneous at this resolution.

Large increases to both floating potential and electron temperature were found when Top-launch RF power was on. Fitting revealed a bulk electron temperature of about 10 eV, which would increase during RF pulses up to about 20 eV in both the upstream and downstream probes, before decreasing again in the absence of RF power. Downstream signals of ion saturation current, electron density and the coefficient of the linear component all responded to RF power in a similar fashion. Upstream signals, except occasionally for electron temperature, appeared largely

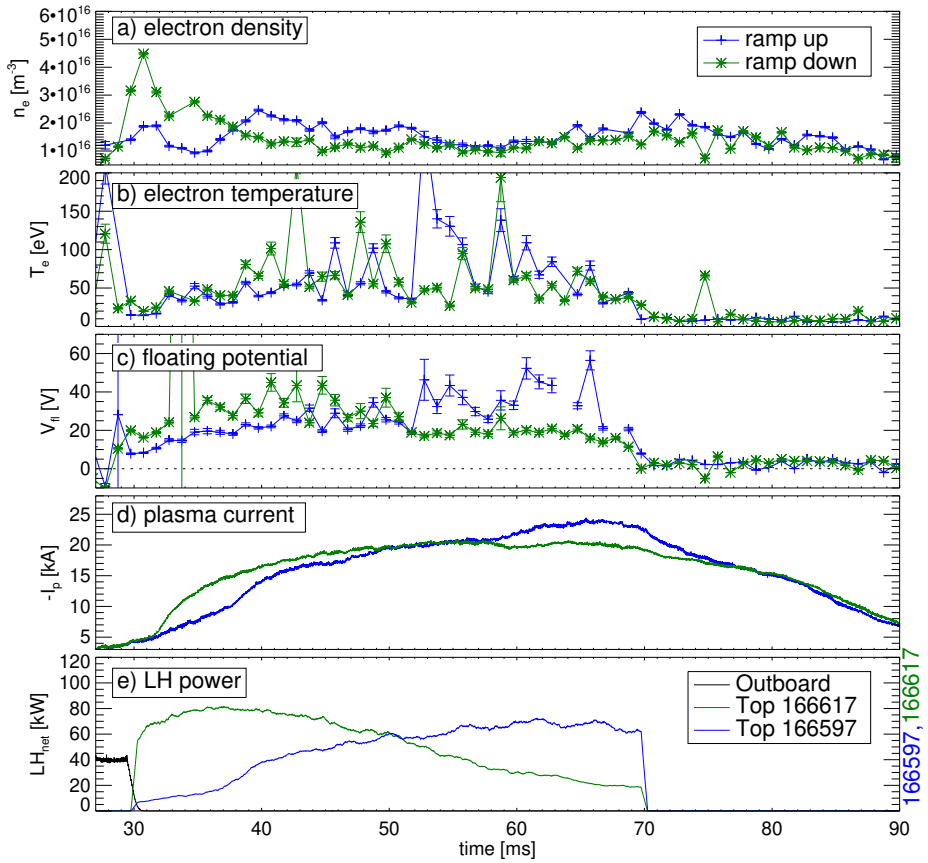

Figure 4.9: Langmuir Probe measurements from the new probe taken during Top-launch discharges (ramp up: #166597, down: #166617). Plasma conditions of a) electron density n_e, b) electron temperature T_e and c) floating potential V_{fl}, as well as d) plasma current I_p and e) injected LH power from the Outboard- and Top-antennae in black and blue/green, respectively.

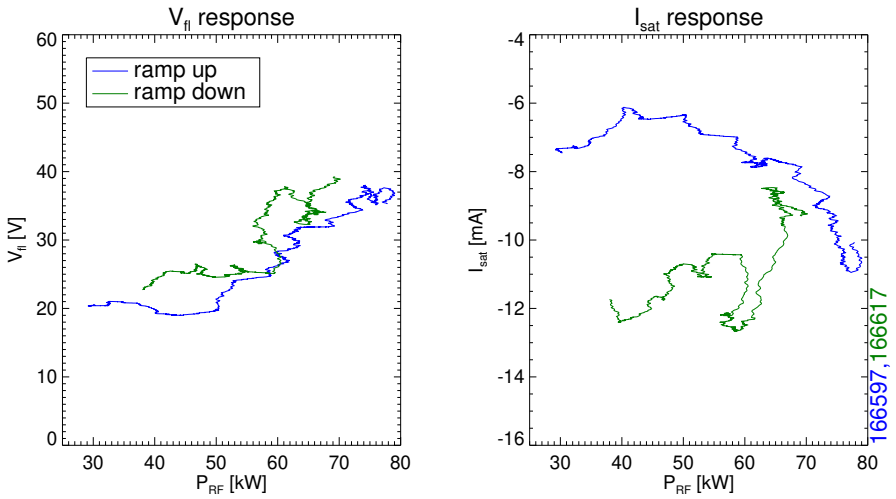

Figure 4.10: Comparison of the temporal response of the floating potential V_{fl} and ion saturation current I_{sat} to RF power P_{RF} using the results presented in Fig. 4.9.

unresponsive. The linear coefficient was smaller for the upstream probe than the downstream probe. Downstream electron density was larger than upstream density by about 50%.

4.4 Non-thermal I-V Response

4.4.1 Linear Offset Model

The I-V characteristics for the discharge shown in Fig. 4.11 are shown in Fig. 4.12. There is a clear deviation of the measured I-V characteristic from the thermal model: a linear component that extends beyond the swept bias (-140 V). The bulk plasma component can still be observed near the floating potential: represented by the exponential component. This caused poor fitting of bulk plasma using the thermal model in the presence of RF power. To obtain the bulk component, a model function combining linear offset and exponential components was applied:

$$I(V) = I_{\text{sat}} + \Delta I V + C \exp\left(\frac{eV}{T_{\text{e}}}\right) \tag{4.3}$$

A linear component was not observed in I-V characteristics shown in Figs. 4.3,

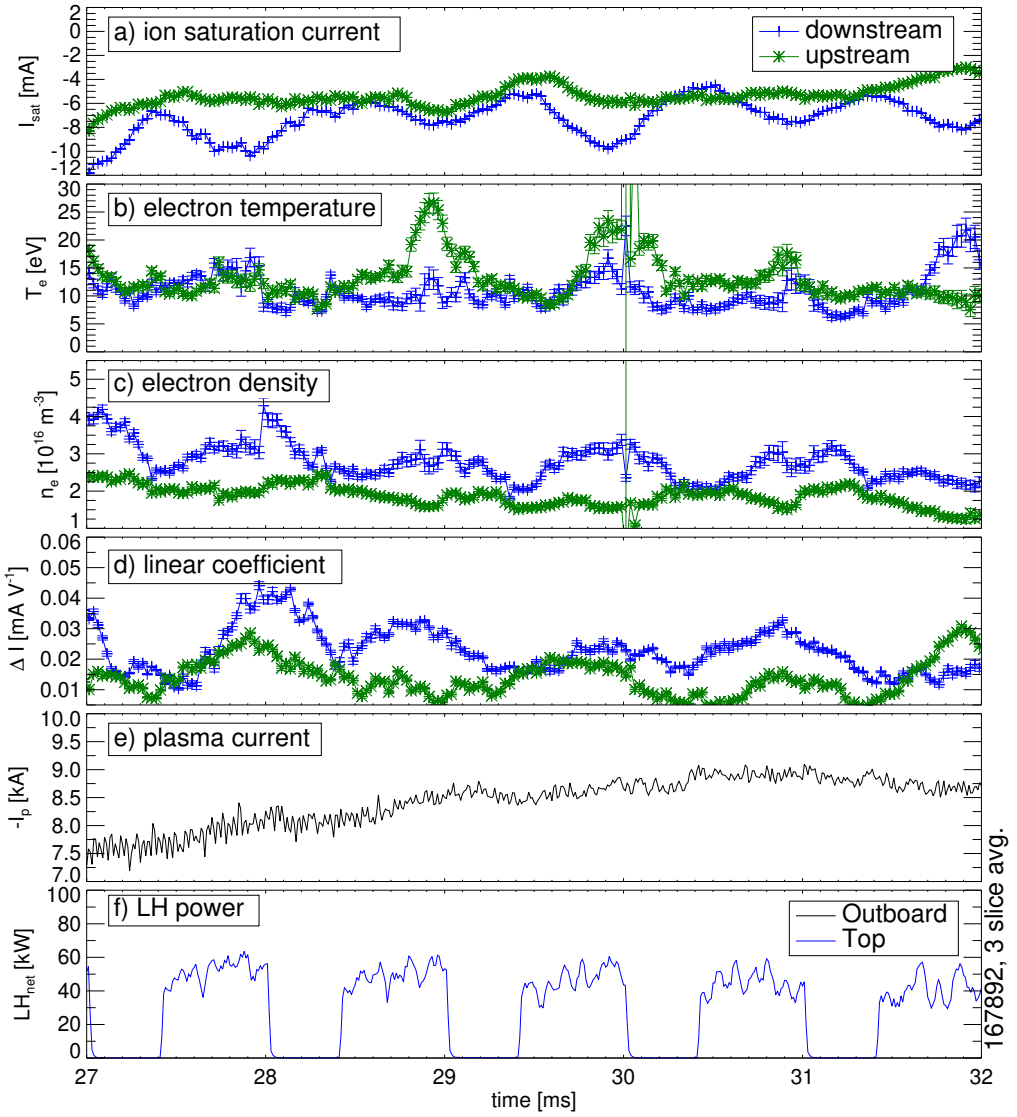

Figure 4.11: Results obtained applying a linear offset model to shot #167892. Plasma conditions of a) ion saturation current I_{sat}, b) bulk electron temperature $T_{\mathrm{e,s}}$, c) electron density n_{e} and d) linear coefficient ΔI defined in Eq. (4.3), as well as e) plasma current and f) injected LH power from the Outboard- and Top-antennae in black and blue, respectively.

4.4, and 4.7. It is unclear why the deviation from the thermal response was so prominent for this discharge specifically. One possibility is a difference in the location of the plasma; the plasma was substantially shifted downwards towards the probe compared to normal operations. As such, core plasma was much closer to the probe and may have had a stronger influence than in other shots presented.

4.4.2 Source of the Non-thermal Component

The departure from a purely exponential I-V response is indicative of a response to a non-thermal electron distribution. A more general expression for the electron current is the Langmuir expression of electron current (see Appendix A):

$$I_e(V) = \frac{2\pi eA}{m_e^2} \int_0^\infty (\varepsilon - eV) f(\varepsilon)\, d\varepsilon \tag{4.4}$$

where ε is the electron energy, A is the probe area and $V = V_b - V_p$ is the probe bias relative to the plasma potential V_p. This expression makes no assumption of the electron distribution function, and indicates that a linear response may be caused by a flattened region of the electron distribution function.

The only possible source at such high energies (>100 eV) are the 'fast' electrons generated by LHCD. As noted in Sec. 1.3, the electron Landau damping of LH waves produces a 'plateau' of flattened electron distribution at high energies as described by Fisch [5]. This described a distribution flattened by a step function $D(\varepsilon)$ in the LHW absorption region in velocity space $w_1 < w < w_2$ and Maxwellian elsewhere.

$$f = C \exp\left(- \int^w \frac{w}{1 + w^3 D(w)}\, dw \right), \tag{4.5}$$

where w is the electron velocity normalized to thermal velocity v_{th}. To investigate the effect a fast electron plateau may have on the probe response, Fisch's model was numerically integrated following Eq. (4.4) to elucidate the structure of the I-V characteristic formed. A parameter scan of variables w_1 and w_2 was performed, using a bulk electron temperature of $T_\mathrm{e} = 10$ eV, the results of which are shown in Fig. 4.13. The fraction of fast electrons to bulk electrons was also evaluated as $f_n = n_{e,f}/n_{e,s}$.

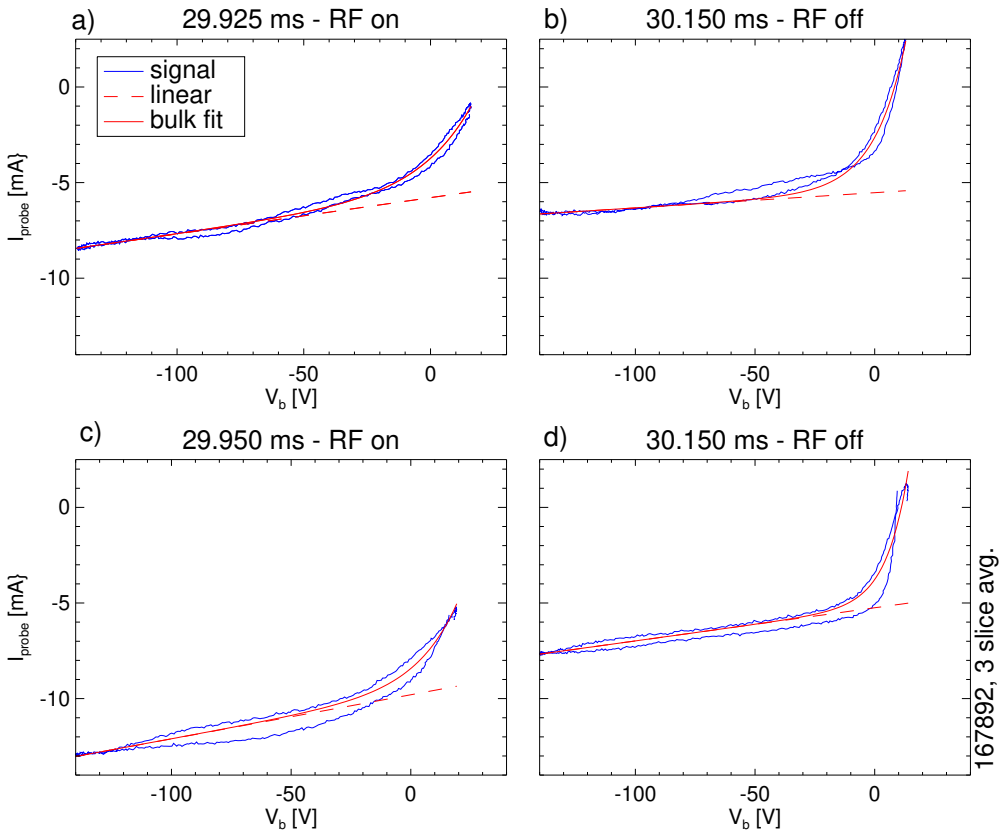

Figure 4.12: Comparison of I-V characteristics from a-b) upstream and c-d) downstream probes during RF-on and -off phases, respectively. I-V characteristics were obtained from shot #167892 with a 40 kHz sweep frequency and 3 slice boxcar averaging applied. Red dashed lines show the fitted linear offset, and solid curves show the fitted results of the model described by (4.3).

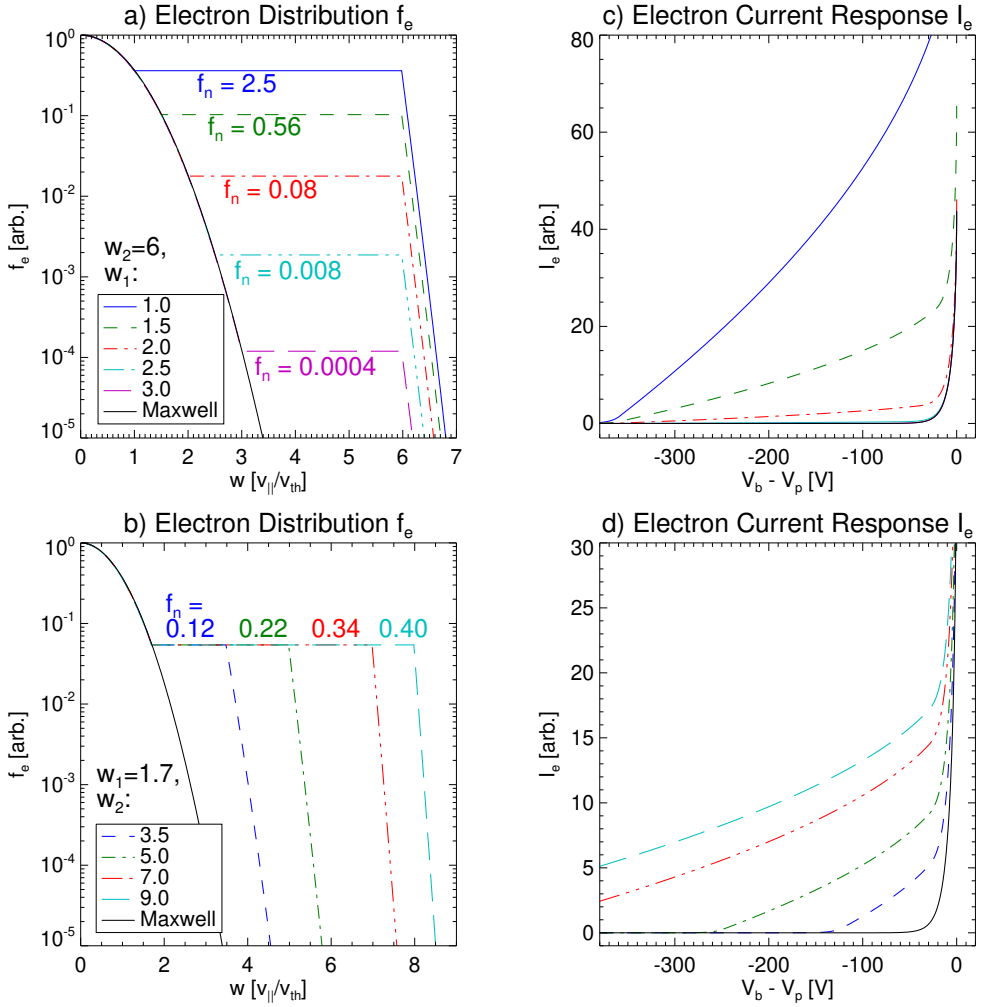

Figure 4.13: The effect of a-b) model electron energy distributions f_e on c-d) probe electron current I_e calculated numerically using Eq. (4.4). Scans of a), c) w_1 and b), d) w_2 are presented.

The calculated electron currents show a strong linearity in the region of wave absorption $w_1 < w < w_2$. The electron current showed a strong dependence on plateau height, reflected by w_1 in its determination of where the plateau meets the bulk distribution. At very small plateau heights ($w_1 > 2.0$, f_n <5%), very little deviation from the thermal response was seen. Such a small alteration would be practically indistinguishable experimentally. For larger plateau heights ($w_1 < 2.0$, f_n >10%), extraordinary deviation from a purely thermal response was seen. The scan of w_1 showed that the height of the plateau determined the slope of the linear component of the electron current, with larger plateau heights corresponding to larger linear coefficients. Scans of w_2 showed a clear influence on the fraction of fast electron, mainly reflecting the beginning of the linear region. However, no correlation was seen between w_2 and the slope of the linear component. The strong resemblance of measured and simulated curves indicates that the linear component of the I-V characteristic may be caused by a fast electron plateau driven by LHCD. Fast electrons can be generated locally in SOL plasma above the LH cut-off density (0.5×10^{15} m^{-3}). According to results in Fig. 4.8, LHW may be able to propagate a large distance into the SOL plasma, giving a large volume in which SOL absorption may occur. However, the linear component observed implies a fast electron fraction of greater than 5%: larger than can be attributed to local absorption of waves alone. Fast electrons generated in the core may also be transported to the SOL through collisions, turbulence, and RF driven diffusion [25], and may produce larger populations of fast electrons.

Chapter 5

Conclusions and Future Work

A new Langmuir Probe has been designed and installed in TST-2. This probe was tested and used to measure SOL conditions at the bottom of TST-2's SOL. The measured electron density n_e was similar to the value observed at different poloidal locations with the previous probes, with typical values of 1.0×10^{16} m^{-3} during both Outboard- and Top-antenna driven discharges. The increased probe area gave better accuracy of n_e measurements due to the improved signal-to-noise ratio of ion saturation current. The exponential decay length of radial SOL density was estimated to be 60-80 mm, corresponding to a LHW cut-off layer 200-400 mm outside of the limiter edge during a Top-launch experiment. In terms of the fast electron flow, both upstream and downstream electron temperature T_e were found to be 8-10 eV in the absence of RF power, and increased to 20 eV during RF power. The measured I-V characteristic showed a clear deviation from a response to thermal plasma, especially on the downstream side. This deviation was characterized as a linear region of the I-V characteristic, which may correspond to a fast electron plateau caused by LHCD. The deviation from the thermal probe response indicates a fast electron population of greater than 5% of the bulk, larger than would be expected from local absorption of LHW. This indicates that the fast electrons detected in the SOL by the downstream probe are mostly transported from the denser core plasma. Probe floating potential V_{fl} increased during RF power for the new probes, indicating the absence of significant RF sheath recti-

fication at the location of the new probes. This is in contrast with the floating potential change observed by the previously installed probes at the top-antenna limiter, which showed large decrease in the floating potential when the nearby antenna was energized.

Future work should aim to clarify the source of the fast electrons in SOL plasma. Temporal analysis of the fast electron population with RF power modulation will be useful in quantifying their source and transport. Electron Energy Distribution Functions (EEDF) could also be obtained directly from probe characteristics [26] (see Appendix B). However, such analysis requires development of the present theory for use in the probe geometry used here. Another method would be to produce an analytic model of the probe's response to a plateau distribution and trialling a fitting function based upon it. Such a model will need to accurately account for the alteration of electron density, temperature and the probe floating potential in the presence of a fast electron population. Finally, isolating the changes in V_{fl} due to RF sheath rectification may help elucidate the effect of fast electrons on the floating potential.

Appendix A

Derivation of the Langmuir Expressions for Probe Electron Current

In the absence of a magnetic field, plasma particle flux Γ is given by

$$\Gamma = \int \upsilon cos\theta f(\boldsymbol{\upsilon})\, d\boldsymbol{\upsilon} \tag{A.1}$$

where $f(\upsilon)$ is the electron energy distribution and

$$d\boldsymbol{\upsilon} = d\boldsymbol{\upsilon}_x d\boldsymbol{\upsilon}_y d\boldsymbol{\upsilon}_z = |\boldsymbol{\upsilon}_x|^2 d\upsilon_x d\Omega, \tag{A.2}$$

where $\upsilon_{x,y,z}$ are the velocity components in Cartesian coordinates. The particle flux in the direction of the probe surface is then

$$\Gamma_x = \pi \int_0^\infty \upsilon_x^3 f(\upsilon_x)\, d\upsilon_x. \tag{A.3}$$

In the isotropic case, $f(\upsilon)$ is Maxwellian, and the resulting electron flux is

$$\Gamma_{e,x} = \pi \int_0^\infty \left(\frac{m_\mathrm{e}}{2\pi T_\mathrm{e}}\right)^{\frac{3}{2}} \upsilon_x^3 \exp\left(-\frac{m\upsilon_x^2}{2T}\right) d\upsilon_x \tag{A.4}$$

$$= \sqrt{\frac{T_\mathrm{e}}{2\pi m_\mathrm{e}}}. \tag{A.5}$$

This results in the same expression as a purely thermal electron collection to a probe that is neutral to surrounding plasma (Eq. (2.14)).

For a negatively biased probe, only electrons whose energy exceeds the probe bias relative to plasma potential $V = V_b - V_p$ are collected by the probe, equivalent to the potential drop across the plasma sheath. Electrons collected by the probe have their energy reduced by this potential:

$$\frac{m\upsilon_e^2}{2} = \frac{m\upsilon_\infty^2}{2} - eV = \varepsilon - eV, \tag{A.6}$$

where the subscripts ∞ and e denote the unreflected electron distribution and distribution collected by the probe, respectively. A relation between the original electron distribution to the one collected by the probe can be obtained by substituting this expression into Eq. (A.3) to obtain

$$\Gamma_e = \frac{2\pi}{m_e^2}\int_{eV}^{\infty}\left(\frac{m_\mathrm{e}}{2\pi T_\mathrm{e}}\right)^{\frac{3}{2}}(\varepsilon - eV)\exp\left(-\frac{\varepsilon - eV}{T}\right)d\varepsilon \tag{A.7}$$

$$= \frac{2\pi}{m_e^2}\exp\left(\frac{eV}{T}\right)\int_{eV}^{\infty}(\varepsilon - eV)f(\varepsilon)\,d\varepsilon \tag{A.8}$$

Thus, the electron current collected by the probe becomes

$$I_e = \frac{2\pi eAn_\mathrm{e}}{m_e^2}\int_{eV}^{\infty}(\varepsilon - eV)f_0(\varepsilon)\,d\varepsilon. \tag{A.9}$$

This is the standard Langmuir expression and makes no assumption of isotropic plasma, thus is the more generally correct expression for electron flux to a negatively biased probe.

The inclusion of a strongly perturbing magnetic field is of interest in measurements using electron currents. As noted in Sec. 2.3, if $\rho_e \ll a < \rho_i$ is satisfied then ion collection remains unperturbed but electron flux reduces to a 1-dimensional flow, thus electron current is inhibited. The derivation of the probe current then requires a kinetic treatment which includes particle diffusion across the magnetic field. Starting from the kinetic equation of isotropic plasma crossing a collisionless sheath,

$$\nabla_r D(\upsilon)\nabla_r f(\varepsilon) = 0 \tag{A.10}$$

where $D(\upsilon) = v^2\lambda/3$ and λ is the electron mean free path. In principle, a full kinetic equation including anisotropy must be considered, but its solution is far from trivial in all situations. Instead, this simplified form may be used if an improved set of boundary conditions is used as follows:

$$f_0(\varepsilon > eV) = \gamma f_1(\varepsilon) \tag{A.11}$$

$$f_1(\varepsilon) = -\lambda \nabla_r f_0(\varepsilon) \tag{A.12}$$

where $f_0(\varepsilon)$ is the isotropic part and $f_1(\varepsilon)$ is the anisotropic part of the EEDF, and γ is the geometric factor. γ varies monotonically from 4/3 to 0.71, depending on magnetic field strength; 4/3 when $\rho_e \gg a$, and 0.71 when $\rho_e \ll a$. Solving Eq. (A.10) with these boundary conditions gives the electron probe current as

$$I_e(V) = \frac{2\pi eA}{m_e^2 \gamma} \int_{eV}^{\infty} \frac{(\varepsilon - eV) f(\varepsilon)}{1 + \frac{\varepsilon - eV}{\varepsilon}\psi}\, d\varepsilon, \tag{A.13}$$

where the diffusion parameter ψ depends on both probe geometry and orientation to the magnetic field. ψ is inversely proportional to ρ_e, thus directly proportional to $|B|$ and inversely proportional to ε. As such, ψ is larger for stronger B_t, but reduced for particles of higher energy. Qualitatively, this is interpreted as reduced I_e from low energy electrons. This represents the distortion in I_e caused by the magnetic field. Conversely, when $\psi \ll 1$, this expression simplifies to Eq. (A.9) as expected.

Appendix B

Electron Energy Distribution Function Analysis

Typical Langmuir probe measurements rely on the presence of isotropic, unmagnetized plasma. If asymmetry in the electron energy distribution is suspected, Electron Energy Distribution Function (EEDF) analysis can be used [26]. The EEDF is a function related to the Electron Distribution Function $F(t, r, \upsilon)$ but neglects information on spacial and temporal changes, focusing only on electron energy $\varepsilon = \frac{1}{2}m\upsilon^2$. Analysing the EEDF can quickly identify any deviation from a Maxwellian distribution, which appears as linear on a semi-log scale in EEDF plots.

EEDF analysis is typically performed by the Druyvesteyn method of probe analysis [27, 28]. $f(\varepsilon)$ is normalized to number density n by

$$\int_0^\infty f(\varepsilon)\, d\varepsilon = n. \tag{B.1}$$

In stable, low density plasma without the strong influence of a magnetic field, the probe electron current is given by the Langmuir expression (Eq. (A.9)) The EEPF

can then be found from the second-derivative of (A.9)

$$I'_e = \frac{2\pi eA}{m_e^2}\frac{d}{dV}\left(\int_{eV}^{\infty} \varepsilon f(\varepsilon)\, d\varepsilon - eV\int_{eV}^{\infty} f(\varepsilon)\, d\varepsilon\right) \tag{B.2}$$

$$= \frac{2\pi eA}{m_e^2}\left[-eVf(eV) - e\int_{eV}^{\infty} f(\varepsilon)\, d\varepsilon + eVf(eV)\right], \tag{B.3}$$

$$= -\frac{2\pi e^2 A}{m_e^2}\int_{eV}^{\infty} f(eV)\, d\varepsilon, \tag{B.4}$$

$$I''_e = -\frac{2\pi e^3 A}{m_e^2} f(eV). \tag{B.5}$$

This gives the EEDF in terms of the second-derivative of the I-V characteristic.

$$f(\varepsilon) = -\frac{m_e^2}{2\pi e^3 A}\frac{d^2 I_e}{dV^2} \tag{B.6}$$

This method is appropriate for use in low pressure plasmas which are unperturbed by the probe diagnostic in the absence of a strong magnetic field.

Bibliography

[1] J. P. Freidberg, *Plasma Physics and Fusion Energy* Cambridge Univ. Press (2007).

[2] R. J. Goldston and P. H. Rutherford, *Introduction to Plasma Physics* Inst. Phys. Pub., London (1995).

[3] Y-K.M. Peng and D.J. Strickler, Nucl. Fusion **26** 769 (1986).

[4] S. Li, H. Jiang, Z. Ren, C. Xu, *"Tokamak principle"* licensed by Wikimedia under Creative Commons 4.0, lastest version 12/07/20. https://commons.wikimedia.org/wiki/File:Schematic-of-a-tokamak-chamber-and-magnetic-profile.jpg

[5] N.J. Fisch and A.H. Boozer, Phys. Rev. Lett. **45** 720–2 (1980).

[6] Y. Takase et al, Phys. Fluids **28** 983–948 (1985).

[7] R. Cesario et al, Nat. Commun. **1** 55 (2010).

[8] B.J. Ding et al, Nucl. Fusion **55** 093030 (2015).

[9] N. Tsujii et al, Nucl. Fusion **57** 126032 (2017).

[10] G.M. Wallace et al, Nucl. Fusion **51** 083032 (2011).

[11] E.H. Martin et al, Nucl. Fusion **59** 076006 (2019)

[12] I.H. Hutchinson, *Plasma Diagnostics*, Cambridge Univ. Press (2005).

[13] P.C. Stangeby, *The Plasma Boundary of Magnetic Fusion, Devices*, Institute of Physics Publishing (2000).

[14] H. M. Mott-Smith and I. Langmuir, Gen. Elec. Rev., **27** 617 (1924).

[15] J. C. Xu et al, J. INST. **14** P06028, (2019).

[16] L. Nie et al, Nucl. Fusion **58** 036021, (2018).

[17] H. W. Müller et al, Nucl. Fusion **51** 073023, (2011).

[18] J. A. Boedo, Physics of Plasmas **8** 4826, (2001).

[19] R.J. Perkins et al, Nucl. Mater. Energy **12** 283-288 (2017).

[20] Tsv.K. Popov et al, Plasma Sources Sci. Technol.

[21] Y. Takase et al, Nucl. Fusion, **41** 1543 (2001).

[22] J. H. P. Rice et al, Plasma Fus. Res., **15**, 2402009 (2020).

[23] T. Shinya et al, Nucl. Fusion, **57** 036006 (2017).

[24] T. Shinya, *Non-Inductive Plasma Current Ramp-up on the TST-2 Spherical Tokamak Using the Lower Hybrid Wave*, The University of Tokyo, Japan (2015).

[25] A. Kaufman, Physics of Fluids, **15** 1063 (1972)

[26] Tsv.K. Popov et al, Plasma Sources Sci. Technol. **25** 033001 (2016).

[27] M. J. Druyvesteyn, Z. Phys., **64** 781–98 (1930).

[28] V.A. Godyak and V.I. Demidov, J. Phys. D: Appl. Phys. **44** 233001 (2011).